Quantitative Imaging of the Electrostatic Field and Potential Generated by a Transmembrane Protein Pore at Subnanometer Resolution

ARTICLE *in* NANO LETTERS · SEPTEMBER 2013

Impact Factor: 13.59 · DOI: 10.1021/nl403232z · Source: PubMed

3 AUTHORS:

Moritz Pfreundschuh
ETH Zurich
8 PUBLICATIONS **46** CITATIONS
SEE PROFILE

Ulf Hensen
ETH Zurich
22 PUBLICATIONS **390** CITATIONS
SEE PROFILE

Daniel J Müller
ETH Zurich
255 PUBLICATIONS **12,926** CITATIONS
SEE PROFILE

NANO LETTERS

Letter

pubs.acs.org/NanoLett

Quantitative Imaging of the Electrostatic Field and Potential Generated by a Transmembrane Protein Pore at Subnanometer Resolution

Moritz Pfreundschuh, Ulf Hensen, and Daniel J. Müller*

Department of Biosystems Science and Engineering, ETH Zurich, CH-4058 Basel, Switzerland

Supporting Information

ABSTRACT: Elucidating the mechanisms by which proteins translocate small molecules and ions through transmembrane pores and channels is of great interest in biology, medicine, and nanotechnology. However, the characterization of pore forming proteins in their native state lacks suitable methods that are capable of high-resolution imaging (~1 nm) while simultaneously mapping physical and chemical properties. Here we report how force−distance (FD) curve-based atomic force microscopy (AFM) imaging can be applied to image the native pore forming outer membrane protein F (OmpF) at subnanometer resolution and to quantify the electrostatic field and potential generated by the transmembrane pore. We further observe the electrostatic field and potential of the OmpF pore switching "on" and "off" in dependence of the electrolyte concentration. Because electrostatic field and potential select for charged molecules and ions and guide them to the transmembrane pore the insights are of fundamental importance to understand the pore function. These experimental results establish FD-based AFM as a unique tool to image biological systems to subnanometer resolution and to quantify their electrostatic properties.

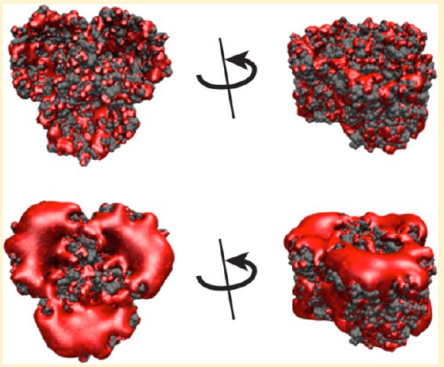

KEYWORDS: *Force-volume AFM, electrostatic interactions, multiparametric imaging, nanopore, surface charge*

The transport of ions and molecules across cellular membranes is essential for many processes of life. Therefore, understanding of this transport finds broad interest in biology and medicine and is required to engineer synthetic nanopores.[1−5] From atomic-resolution structures determined for proteins forming transmembrane pores, channels and pumps we begin to understand the architecture and mechanism of selective molecular transport.[1,2,6] To be specifically transported across the cellular membrane ions and molecules have to undergo a subset of physical and chemical interactions. Among these electrostatic interactions take essential roles.[6−8] The electrostatic properties of transmembrane proteins can be calculated and visualized using three-dimensional (3D) structural models. However, so far no experimental method exists that can image native proteins at subnanometer resolution and at the same time probe their electrostatic properties in vitro. Such a method would be of particular interest to image transmembrane pores or channels and to structurally localize and to quantify the electrostatic fields that translocate molecules, ions, ligands, or proteins.

Since its invention, atomic force microscopy (AFM)[9,10] has been applied to image the surface of native membrane proteins at subnanometer resolution.[11−14] Because AFM can record topographs in buffer solution and at ambient temperature it enables the observation of single membrane proteins at work.[14,15] Examples comprise the surface-layer from *Deinococcus radiodurans*,[16] connexins forming animal communication channels in epithelial cells,[17,18] the light-driven proton pump bacteriorhodopsin,[19,20] the cyclic nucleotide-regulated and the pH-gated potassium channel,[21,22] the ATP-gated purinergic receptor $P2X_4$,[23] and the outer membrane proteins (Omps) OmpG and OmpF from *Escherichia coli*.[24,25] Although such AFM imaging studies bring exciting insight into the structure−function relationship of membrane proteins, the understanding of how membrane proteins work requires gathering additional information. Interestingly, within the past decade AFM has been developed toward a multifunctional nanotool that allows quantifying structural, biophysical, and chemical properties of biological systems.[10,26]

The so-called force−distance (FD) curve-based AFM (FD-based AFM; also called force-volume AFM (FV-AFM)) contours a sample surface while approaching pixel-by-pixel AFM tip and sample to record FD curves (Supporting Information Figure S1a,b).[27−30] Analyzing such FD curves allows the mechanical and electrostatic properties of the sample to be determined and mapped to the sample topography.[29,31] For more than a decade, FD-based AFM has suffered from technical limitations such as slow imaging speed, limited number of pixels, poor force resolution (~0.1−1 nN), and poor spatial resolution (~10−100 nm).[29] Recent advances pushed the limits of FD-based AFM to detect biological forces in the

Received: August 29, 2013
Revised: September 24, 2013
Published: September 30, 2013

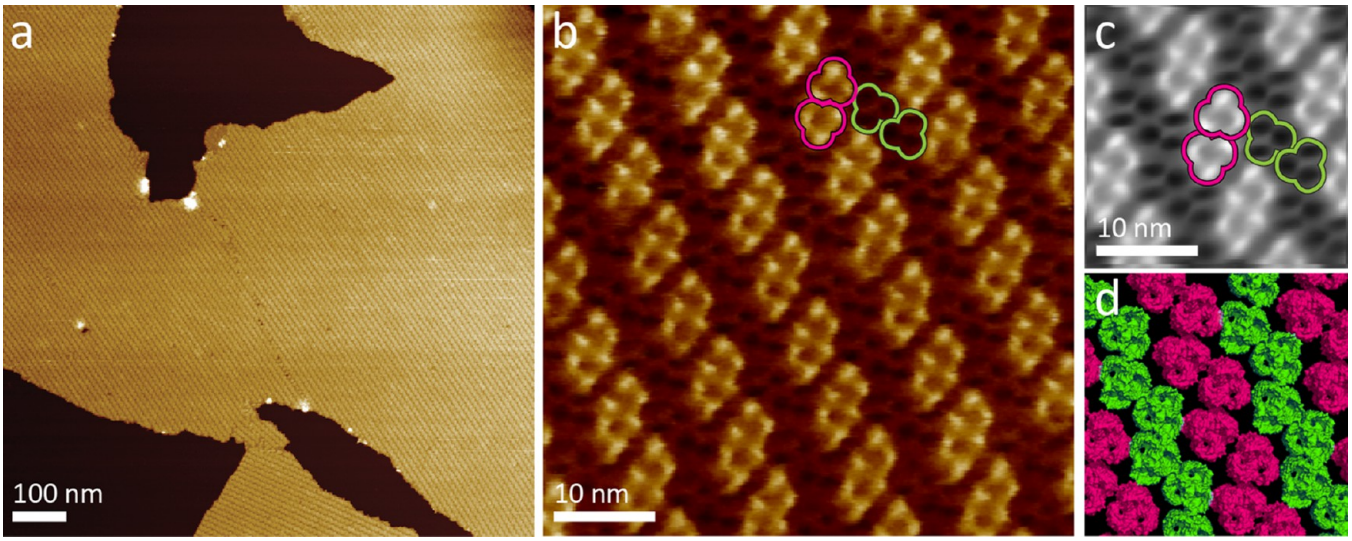

Figure 1. FD-based AFM topographs of native OmpF trimers reconstituted into lipid membranes. (a) FD-based AFM topograph showing an OmpF membrane adsorbed onto mica. OmpF membranes protruded 7.0 ± 1.0 nm (n = 60) from the supporting mica. (b) Higher-magnification topograph revealing OmpF trimers assembled into two-dimensional crystalline arrays. (c) Cross-correlation averaged and symmetrized OmpF trimers recorded in (b). OmpF trimers exposing their extracellular (purple line) and periplasmic (green line) surface are outlined. Full color ranges correlate to vertical scales of 15 (a), 2.0 (b), and 1.7 nm (c). FV-AFM topographs were recorded in buffer solution (300 mM KCl, 10 mM Tris-HCl, pH 7.4) applying an imaging force of 150 pN. (d) Model showing the packing of OmpF trimers imaged in (c). Purple OmpF trimers expose the extracellular surface and green trimers expose the periplasmic surface. OmpF trimers (PDB file 1OPF)[40] were arranged using Pymol. OmpF trimers have been reconstituted into lipid (DMPC) membranes (Materials and Methods).

pN regime at a spatial resolution approaching 1 nm and at imaging times approaching that of conventional AFMs (~8 min for 512 × 512 pixels).[32−36] Owing to these developments FD-based AFM is increasingly used to characterize the mechanical properties of biological samples.[30] In this work, we introduce FD-based AFM to image single membrane proteins and at the same time to structurally map the electrostatic field and potential generated by their transmembrane pore. The experiments demonstrate that FD-based AFM can be used to quantify the electrostatic properties of native protein surfaces at subnanometer resolution.

Results and Discussion. *FD-Curves Detect Mechanical and Electrostatic Properties of Biological Samples.* FD curves recorded by AFM describe a mechanical process (Supporting Information Figure S1a,b). For this reason, in the majority of cases FD curves are taken to measure mechanical properties of a sample. For example, indenting an AFM tip into a soft biological sample repels the tip in a distinct way. Measuring this repulsion allows to quantify the deformation of the sample (Supporting Information Figure 1c). Depending on the analysis of FD curves many other mechanical properties of the sample can be quantified.[29,31] In the aqueous solution, the surfaces of the AFM tip and of most biological systems are charged.[7,37] As both surfaces approach they electrostatically repel each other if their surface charges are of the same sign. More than two decades ago it was shown that the electrostatic repulsion between AFM tip and sample can be measured by recording FD curves (Supporting Information Figure 1d). This repulsion can be used to quantify the surface charge of the AFM tip or of a point on the biological sample.[31,38,39] In principle, this electrostatic repulsion could be used to structurally localize the electrostatic properties of native proteins using FD-based AFM.[29,31,39] Moreover, FD-based AFM can quantify and map this repulsion directly in the so-called deformation channel (Supporting Information Figure 1d). However, until now quantifying the electrostatic interactions of complex biological samples at subnanometer resolution has been hampered by technological and methodological limitations.[30] In the following, we apply FD-based AFM to image native membrane proteins at high-resolution and to quantify and visualize their electrostatic properties.

FD-Based AFM Imaging of Native OmpF. As sample we have chosen the OmpF from *E. coli* because its structure and function has been well studied and its transmembrane pore displays unique electrostatic features.[40−42] OmpF is a transmembrane β-barrel protein that naturally exists as trimer. Each β-barrel, folded from 16 antiparallel β-strands, forms a transmembrane pore through which hydrophilic solutes up to ~600 Da can freely diffuse.[42,43] The translocation rate of the pore is linearly related to the solute concentration. However, the cation selectivity of the transmembrane pore increases with decreasing electrolyte concentration.[44] This selectivity originates from charged amino acids, which line the inner constriction of the transmembrane pore and generate an electrostatic potential the strength of which depends on the electrolyte concentration of the aqueous solution.[43,45−47] Whereas the negative electrostatic potential generated by the OmpF pore is greatest in the absence of electrolyte it becomes increasingly screened as the electrolyte concentration rises.

To characterize OmpF by FD-based AFM the trimeric membrane proteins were purified (Supporting Information Figure S2), reconstituted into lipid membranes, and adsorbed onto freshly cleaved mica in buffer solution.[48] The OmpF membranes were then imaged in buffer solution by FD-based AFM (Figure 1). To suppress most of the electrostatic repulsion between the AFM tip and the OmpF membrane the pH and electrolyte concentration of the buffer solution were chosen pH 7.4 (10 mM Tris-HCl) and 300 mM KCl.[49] At low magnification, membrane patches of densely packed OmpFs were observed (Figure 1a). At higher magnification,

dx.doi.org/10.1021/nl403232z | Nano Lett. 2013, 13, 5585−5593

the supramolecular assembly of the OmpF trimers became visible (Figure 1b,c) showing the alternating rows of trimers exposing either their periplasmic or extracellular surface (Figure 1d).

Subnanometer Imaging and Mapping Mechanical Properties of OmpF. Next, we increased the lateral and vertical resolution of the FD-based AFM topographs. The imaging feedback parameters (Materials and Methods) were iteratively optimized until the surface of the native OmpF trimers could be contoured at a force sensitivity of ±7 pN, the AFM topographs revealed finest structural details, and the error force signal was minimized. The pixel size of the AFM topographs was ~0.3 × 0.3 nm^2 to enable a lateral resolution <1 nm. At the optimized imaging force of ~150 pN, the AFM tip contoured in great detail the alternating rows of OmpF trimers exposing either their periplasmic or extracellular surface (Figure 2a). The

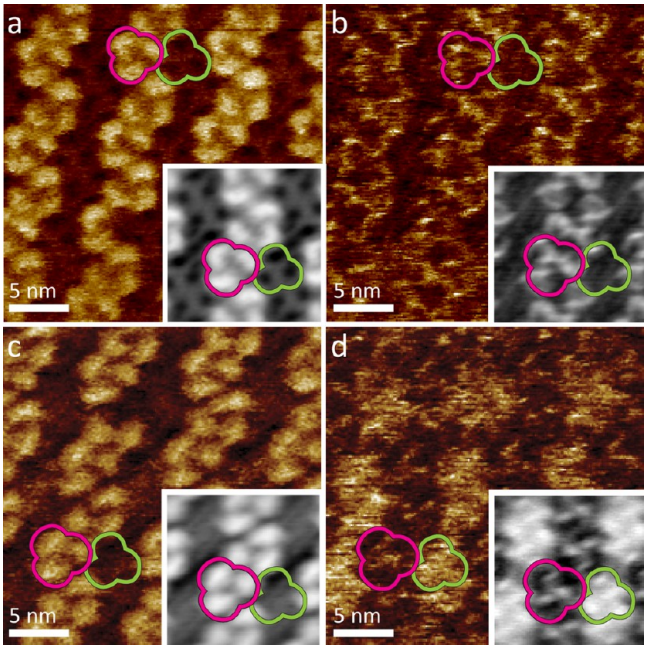

Figure 2. High-resolution FD-based AFM of native OmpF trimers recorded at different electrolyte concentrations. Topograph (a) and deformation map (b) of OmpF trimers recorded in "high" electrolyte concentration (300 mM KCl, 10 mM Tris-HCl, pH 7.4). OmpF trimers reconstituted in a lipid (DMPC) membrane exposed their extracellular (purple line) and periplasmic (green line) surface. Topograph (c) and deformation maps (d) of the same OmpF membrane but recorded in "low" electrolyte concentration (20 mM KCl, 10 mM Tris-HCl, pH 7.4). Insets show 2-fold symmetrized cross-correlation averages (n = 60) of OmpF trimers. FD-based AFM topographs were recorded applying an imaging force of 150 pN. Full color ranges correspond to vertical ranges of 1.6 (a,c), 0.5 (b), and 1.2 nm (d). Deformation values give the difference of the tip sample-distances recorded at 150 and 45 pN.

long extracellular polypeptide loops of the OmpF trimer protruded 1.3 ± 0.2 nm (average ± SD; n = 50) from the lipid membrane, whereas the doughnut-like entrances surrounding the transmembrane pores protruded 0.5 ± 0.1 nm (n = 30). Cross-correlation averaged topographs showed the long extracellular loops of the OmpF trimers and the periplasmic doughnut-like entrance of the transmembrane pores more clearly (Figure 2a). The resolution of these FD-based AFM topographs, as estimated from structural details of single OmpF trimers, approached ≤1 nm.

To optimize the signal-to-noise ratio of the deformation map, deformation values were recorded applying forces ranging from 45 to 150 pN to the OmpF membrane. The lower force threshold of 45 pN was chosen to clearly lie above the noise (~10−20 pN) of the FD curves. Consequently, the deformation value represented the difference of the tip−sample distances recorded at 45 pN and at the imaging force of 150 pN (Supporting Information Figure S1c). Correlation of the FD-based AFM topograph and the simultaneously recorded deformation map revealed a slightly enhanced deformation for OmpF trimers exposing their extracellular surface (~0.4 ± 0.1 nm, n = 40) compared to OmpF trimers exposing their periplasmic surface (~0.2 ± 0.1 nm, n = 40, Figure 2b). The maximum deformation of 0.4 nm localized at the long and flexible extracellular polypeptide loops that protruded 1.3 nm from the lipid bilayer.

The high-resolution FD-based AFM topographs were in excellent agreement with topographs determined earlier by high-resolution contact-mode AFM and with the atomic structure of the OmpF trimer.[13,14,24] The heights detected for the extracellular and periplasmic loops, each of which connecting two β-strands forming the transmembrane β-barrel, were within ±0.2 nm of those measured from high-resolution contact mode AFM topographs and the atomic structure of the OmpF trimer.[13,14,24] This demonstrates that providing the imaging parameters are adjusted appropriately the structurally flexible domains of native membrane proteins can be contoured at subnanometer resolution using FD-based AFM. However, the periplasmic loops deformed to a lesser extent (~0.2 nm) than the long extracellular polypeptide loops (~0.4 nm). These deformation values suggest that the protein was only slightly deformed. Averaged topograph and deformation map of the OmpF trimer (Figure 2a,b) showed that the slightly enhanced deformation at the extracellular surface was localized at the inner vestibule formed by the three extracellular loops of the OmpF trimer. Previous AFM measurements showed that these extracellular loops exhibit an enhanced structural flexibility that allows them to reversibly collapse onto the OmpF pore.[24] This collapse has been suggested to close and gate the transmembrane OmpF pore. A similar closing mechanism induced by extracellular loops was observed to gate the transmembrane pore formed by the β-barrel forming outer membrane proteins OmpG[25,50] and maltoporin (LamB)[51] from *E. coli*. These insights lead to the speculation that the deformation map recorded of the extracellular OmpF trimer surface locates the functionally relevant structural flexibility of the extracellular loops.

In summary, the high-resolution FD-based AFM topographs showed that the flexible polypeptide loops of the extracellular surface of the OmpF trimer can be contoured in their fully protruding state (Figure 2a). In addition the doughnut-like periplasmic entrance of the transmembrane pore was contoured in great detail. This demonstrated that the conditions used to record high-resolution FD-based AFM topographs allow the observation of native OmpF trimers in the minimally perturbed state.

Detecting Electrostatic Interactions of OmpF at Subnanometer Resolution. Amino acid residues lining the constriction of the transmembrane OmpF pore can generate a predominantly negative electrostatic potential that promotes the transport of cations and of positively charged molecules.[43−46]

dx.doi.org/10.1021/nl403232z | *Nano Lett.* 2013, 13, 5585−5593

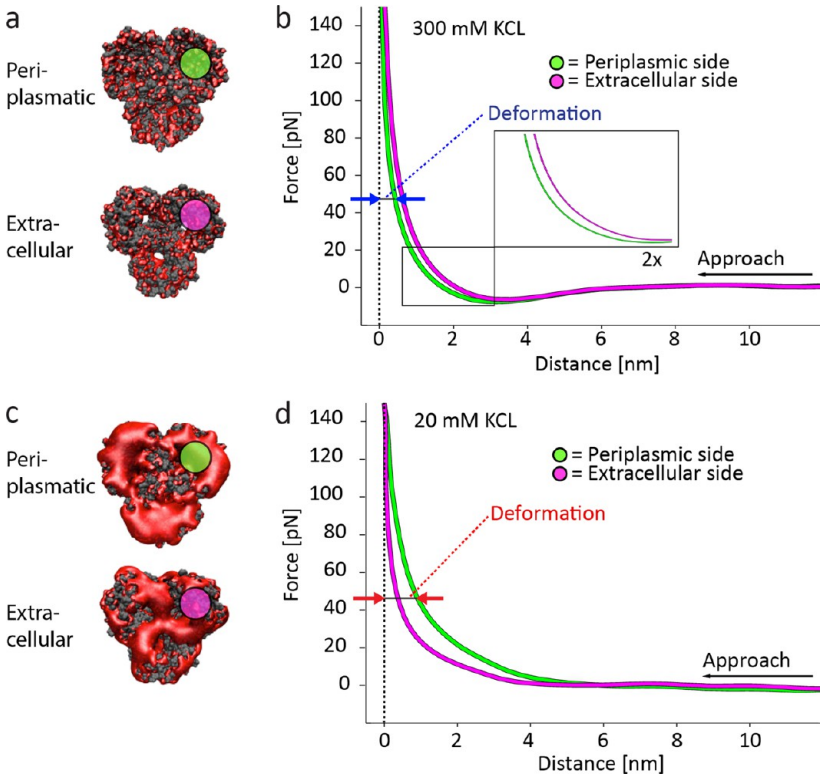

Figure 3. Electrostatic potential calculated and electrostatic repulsion measured of OmpF trimers embedded into the lipid membrane. (a,c) Electrostatic potential calculated based on the atomistic model of the OmpF trimer (PDB 1OPF)[40] embedded in a lipid (DMPC) membrane (Supporting Information Figure S3). For clarity lipids are not shown. The electrostatic potentials calculated for aqueous solutions containing 300 (a) and 20 mM (c) monomeric electrolyte are displayed as equipotential surfaces at ∼−77 mV. Side views of OmpF trimers and other equipotential values are displayed in Supporting Information Figure S4. Green and purple circles indicate the regions from which FD-curves were extracted from FD-based AFM topographs (Figure 2). (b,d) FD curves recorded either on the periplasmic or the extracellular surface of OmpF trimers imaged in Figure 2. FD curves have been recorded in buffer solution containing either 300 mM KCl (b) or 20 mM KCl (c) at pH 7.4. Each FD curve represents the average of 100 FD curves (Supporting Information Figure S5). At low electrolyte concentration, the increasing electrostatic repulsion between the AFM tip and the periplasmic surface of OmpF porin significantly alters the shape of the FD curve (comp. Supporting Information Figure S1d). FD-AFM records this electrostatic repulsion as "deformation". Deformation values indicated by blue (b) and red (d) arrows give the difference of the tip sample-distances recorded at 150 pN and at 45 pN, which are mapped in the deformation maps (Figure 2).

At sufficiently high electrolyte concentration, for example at 300 mM KCl at neutral pH, this electrostatic potential is largely screened and the charge selectivity of the pore disappears. However, at an electrolyte concentration of 20 mM KCl the negative electrostatic potential established by the transmembrane pore is sufficiently strong to repel anions and to preferentially transport cations.[43,46,47] As with an anion, the silicon AFM tip carries a negative charge at neutral pH and if the transmembrane pore of OmpF establishes a sufficiently strong negative electrostatic potential the AFM tip will be electrostatically repelled.[38,39,47] To see whether this electrostatic repulsion can be detected by FD-based AFM we recorded the same OmpF trimers, which have been before imaged at 300 mM KCl, at 20 mM KCl (Figure 2c). The high-resolution FD-based AFM topograph recorded at 20 mM KCl (Figure 2c) showed very similar structural details to the topograph recorded at higher electrolyte concentration (Figure 2a). However, the deformation map recorded at low electrolyte concentration showed significantly increased values of 1.2 ± 0.1 nm (n = 50) at the periplasmic pores of the OmpF trimer (Figure 2d), whereas the deformation detected at the long and flexible polypeptide loops of the extracellular surface did not change (0.4 ± 0.1 nm; n = 50).

In summary, the correlation of FD-based AFM topographs with deformation maps showed that at low electrolyte concentration the OmpF trimer did not change structure but that the transmembrane pores at their periplasmic surface generated considerable deformation maxima of 1.2 nm. These deformation maxima quantify the repulsion between the AFM tip and the transmembrane OmpF pore (Figure 1d). The atomic model of the OmpF trimer shows that the periplasmic pores are open and cannot be structurally occluded.[40] In addition, the high-resolution topographs of the OmpF trimers do not indicate any deformation in the range of ∼1.2 nm. Therefore, we conclude that the electrolyte dependent repulsion detected at the transmembrane pore is not related to structural changes.

Characterizing the Electrostatic Repulsion of the Transmembrane Pore. To better understand the origin of the electrolyte-dependent deformation detected at the transmembrane OmpF pore we calculated the electrostatic potential generated by the OmpF trimer. For this, we have set up an atomistic model of the OmpF trimer embedded into a DMPC bilayer (Supporting Information Figure S3) and computed the equipotential surfaces of the electrostatic potential by solving the Poisson−Boltzmann equations (Figure 3 and Supporting Information Figure S4). At 300 mM monovalent electrolyte, the negative electrostatic potential generated by the pore is rather weak and remains localized to the protein surface (Figure 3a). However, at 20 mM monovalent electrolyte the negative

dx.doi.org/10.1021/nl403232z | *Nano Lett.* 2013, 13, 5585−5593

electrostatic potential generated by the pore became much stronger and protruded into the aqueous solution (Figure 3c). The electrostatic potential extended into the solution much further from the periplasmic surface than from the extracellular surface. In contrast, the electrostatic potential at the extracellular surface remained inside the vestibule formed by the long extracellular loops (Supporting Information Figure S4).

A negatively charged AFM tip interacting with a negative electrostatic potential such as generated by the OmpF trimer will be electrostatically repelled.[31,38,39,47,49] If sufficiently large, this repulsive interaction can be detected by recording FD curves between AFM tip and sample. As FD-based AFM records these FD curves for every pixel of the sample topograph we extracted FD curves from our high-resolution topographs for further analysis (Figure 3). Because single FD curves can vary considerably we averaged 100 FD curves recorded at the periplasmic pore and 100 FD curves recorded at the extracellular loops (Supporting Information Figure S5). At high electrolyte concentration (300 mM KCl), FD curves recorded at the extracellular surface showed a slightly enhanced repulsion compared FD curves recorded at the periplasmic surface (Figure 3b). This was expected from high-resolution deformation maps that detected enhanced values at the structurally flexible extracellular loops (Figure 2b). When lowering the electrolyte concentration to 20 mM KCl the FD curves recorded on the extracellular surface of the OmpF trimer showed no significant change (Figure 3d). In contrast, FD curves recorded at the periplasmic pore detected a significantly enhanced repulsion. This repulsion was fully reversible and only depended on the electrolyte concentration of the buffer solution (at pH 7.4). At low electrolyte concentration (20 mM KCl), the repulsion detected at the periplasmic pore was maximal whereas at high electrolyte concentration (300 mM KCl) the repulsion disappeared.

In a nutshell, the combination of simulations and FD curves revealed that at low electrolyte concentration the OmpF trimer generates significant electrostatic repulsion at the periplasmic pore. In FD-based AFM, this repulsion was detected as deformation maximum above the periplasmic OmpF pore (Figure 2c,d).

Visualizing and Quantifying the Electrostatic Field and Potential Generated by the Transmembrane Pore. Superimposing the deformation map and AFM topograph of the OmpF trimers shows clearly that with decreasing electrolyte the electrostatic repulsion contributes to the deformation value (Figure 4). This electrostatic repulsion maximizes above the periplasmic OmpF pore (Figure 4d–f). The atomistic model of the OmpF trimer (Supporting Information Figure S3) shows that the periplasmic pore lacks structural features that could contribute to the increased deformation value detected at low electrolyte concentration and highlight the electrostatic nature of the repulsion quantified. The electrostatic nature of this repulsion is nicely detected by FD curves recorded at the OmpF pore (Figure 3d). In the following, we analyze the repulsive electrostatic force detected at the OmpF pore to quantify the electrostatic field and potential generated by the transmembrane pore.

Using Coulomb's law we can roughly estimate the electrostatic field by dividing the force of the electrostatic repulsion through the net charge Q_{tip} of the AFM tip. Q_{tip} is the surface charge density multiplied with the surface area of the AFM tip. We quantified the surface charge density of the silicon AFM tip

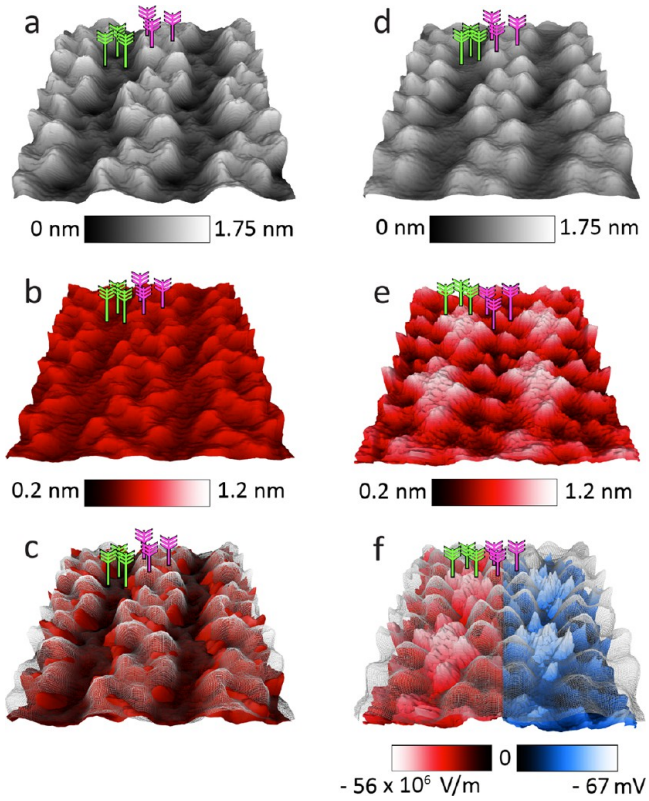

Figure 4. FD-based AFM topographs and deformation maps recorded of the native OmpF trimer localize and quantify the electrostatic field and potential generated by the transmembrane pore. (a) Periplasmic (green arrows) and extracellular (purple arrows) surface of OmpF trimers recorded at high electrolyte concentration (300 mM KCl). Individual periplasmic channel entrances of OmpF are visible (green arrows) whereas the extracellular surface of OmpF protrudes long characteristic polypeptide loops above (~1.3 nm) the surface of the lipid membrane (purple arrows). (b) The deformation map recorded at high electrolyte concentration shows maxima at the structurally flexible extracellular loops (purple arrows) and minima at periplasmic pores (green rows). (c) Superimposition of topograph and deformation map recorded at high electrolyte concentration. (d) Periplasmic (green arrows) and extracellular (purple arrows) surface of OmpF trimers recorded at low electrolyte concentration (20 mM KCl). (e) The deformation map recorded at low electrolyte concentration shows maxima at the periplasmic entrance of the pores (green arrows) whereas the deformation of the structurally flexible extracellular loops remained as detected at 300 mM KCl (purple arrows). The enhanced deformation values recorded at low electrolyte concentration are based on the electrostatic repulsion (Figure 3). (f) Deformation values recorded in the presence of electrostatic repulsion contour the electrostatic field (red) and potential (blue) generated by the OmpF pore. Full color ranges correspond to vertical ranges of 1.7 nm (a,d), 1.2 nm (b,c,e), and −56 × 10^6 V/m (red, f) and −67 mV (blue, f).

by recording FD curves of freshly cleaved mica in aqueous solution containing 3 mM KCl (Supporting Information Figure S6). At such low electrolyte concentration, the electrostatic double layer repulsion between AFM tip and mica can be clearly detected, which allowed to estimate the surface charge density of the AFM tip to −0.032 ± 0.010 C/m^2 (n = 5).[31,39] This value corresponds to the surface charge density (−0.032 C/m^2) previously determined for Si_3N_4 tips.[38] From the spatial resolution of our AFM topographs, we estimated the radius of the AFM tip to be ~2 nm.[52] Approximating the shape of the

dx.doi.org/10.1021/nl403232z | *Nano Lett.* 2013, 13, 5585–5593

AFM tip interacting at high-resolution with the sample to be a half-sphere this yields a total charge of the AFM tip Q_{tip} = $-8.04 \times 10^{-19} \pm 2.51 \times 10^{-19}$ C.[52,53] With the deformation threshold force of ~45 pN used (Figure 3) we can conclude that at low electrolyte concentration (20 mM KCl) the AFM tip contoured the electrostatic field at $-56.0 \times 10^6 \pm 25.4 \times 10^6$ V/m. Because FD-based AFM quantifies the distance at which this field is detected from the pore entrance (~1.2 nm) we can calculate the electrostatic potential generated at the pore entrance to be -67 ± 35 mV. This experimentally approached potential is very similar compared to the negative electrostatic potential calculated from the atomistic OmpF model (Figures 3 and 4 and Supporting Information Figure S4). Although the experimental and calculated values agree remarkably well-improved data analysis and theoretical approaches may in the future provide even more accurate values.

Electrostatic potentials across cellular membranes, including the outer membrane from *E. coli*, typically range from −30 to −100 mV.[42,54,55] With a membrane thickness ranging from 5 to 8 nm such potentials generate electrostatic fields ranging from -4 to -20×10^6 V/m. Thus, the electrostatic field and potential generated by the OmpF pore is of similar range as typically generated across cellular membranes. However, in contrast to the electrostatic field/potential generated across cellular membranes, OmpF generates a structurally localized electrostatic field/potential by charged residues lining the constriction of the transmembrane pore.[43−47] By acting over longer distances, the electrostatic field/potential of every OmpF pore generates electrostatic forces that are able to guide diffusing charged molecules and ions into the vicinity of the transmembrane pore, where short-range interactions (van der Waals, hydrogen, or steric) are able to take hold.[56−58] With decreasing electrolyte concentration this electrostatic field/potential generated by the OmpF pore increases strength, protrudes further from the membrane and interacts over an extended distance/volume with charged solutes. According to the Boltzmann law, an electric potential of −67 mV at the OmpF pore will increase the local concentration of cations by a factor of ~14 compared to the cation concentration of the bulk solution. This increased electrostatic potential may help *E. coli* to accumulate positively charged solutes (including cations) at the OmpF pore for transport across the outer membrane at low electrolyte concentrations (≤20 mM), which occur for example in the lower part of large intestines.

Conclusion. We have visualized and quantified the electrostatic field and potential generated by the transmembrane pore forming protein OmpF using FD-based AFM. The imaging process is sufficiently sensitive to reproducibly image the native surface of OmpF in the lipid membrane at physiological conditions and at subnanometer resolution. The deformation of the structurally flexible OmpF surfaces could be reduced to a minimum of ~0.2 nm. FD-curves are particularly well suited to detect the electrostatic interaction between the AFM tip and a sample. The transmembrane pore of OmpF generates a negative electrostatic field and potential, which is screened at increased electrolyte concentrations but becomes strong at low (or none) electrolyte concentration. Because the AFM tip is also negatively charged an electrostatic repulsion between AFM tip and pore is recorded in FD-curves. Conveniently, FD-based AFM can directly contour the electrostatic field by recording deformation maps. The deformation value quantifies the distance from the protein surface at which the electrostatic field is sufficiently strong to repel the charged AFM tip with a given force (here ~45 pN). Hence the deformation map contours the electrostatic field generated by the transmembrane pore at a given strength. Using the Coulomb's law the electrostatic field strength can be approximated from the electrostatic force and the surface charge of the AFM tip. Furthermore, multiplying the electrostatic field strength by the distance from the pore at which this field strength was detected approximates the electrostatic potential generated by the pore. In principle, the technological approach described here can be applied to structurally map and quantify the electrostatic properties of other biological systems at high resolution. However, its utility might be further explored by using a conductive AFM tip in which electric potential can be modulated.[59] The utility of the approach may be also expanded by chemically modifying the AFM tip to render its surface charge (and chemical properties).[60,61] Using chemical groups that change charge upon photoactivation would, for example, allow the ability to switch the electrostatic properties of the AFM tip and to discern mechanical (uncharged groups) from electrostatic (charged groups) interactions. With such functionalized tips, FD-based AFM could be applied in the future to spectroscopically characterize and structurally map the electrostatic properties of single native membrane proteins at subnanometer resolution. Such structurally resolved quantification of electrostatic properties is not only important to understand transmembrane ion channels and pores but also to characterize many other biomolecular processes, such as cell adhesion, macromolecular assembly, molecular recognition, transport, and signaling.

Materials and Methods. *Purification and Reconstitution of OmpF.* OmpF from *E. coli* was purified by detergent extraction and solubilized in *n*-octylpolyoxyethylene (Octyl POE, 1% w/v, Enzo LifeSciences) as described.[62] Purity of OmpF was verified by SDS-PAGE and silver-staining gels (Supporting Information Figure S2). Solubilized OmpF was reconstituted into 1,2-dimyristoyl-sn-glycero-3-phosphorylcholine (DMPC, Avanti Lipids) by dialysis-driven detergent removal.[63] Briefly, OmpF was mixed with *n*-dodecyl-*N*,*N*-dimethylamine-*N*-oxide (LDAO)-solubilized DMPC (1% w/v, Affymetrix) at a lipid-to-protein ratio of 0.5 (w/w), placed into dialysis buttons and dialyzed against detergent-free buffer (100 mM NaCl, 20 mM HEPES, 10 mM $MgCl_2$, 0.01% [w/v] NaN_3, 0.2 mM dithiothreitol (DTT), pH 7.4) for 6 days at 30 °C. All chemicals used were analytical grade and the water used was ultrapure (>18 MOhm/cm).

High-Resolution FD-Based AFM Imaging. Native OmpF reconstituted into lipid membranes was prepared for AFM as described.[48] Briefly, OmpF membranes were adsorbed onto freshly cleaved mica in buffer solution (300 mM KCl, 10 mM Tris-HCl, pH 7.6). After 50 min of adsorption, the sample was rinsed with the imaging buffer (20 mM KCl or 300 mM, 10 mM Tris-HCl, pH 7.4) and imaged in imaging buffer at room temperature (~22 °C). FD-based AFM imaging was performed using a Bruker Nanoscope Multimode 8 (Bruker, Santa Barbara, USA) equipped with a 120 μm piezoelectric scanner (J-scanner). Rectangular shaped silicon cantilevers (38 μm long) had a sharpened silicon tip with a nominal radius of 8−10 nm, a nominal spring constant of 0.1 N/nm, and a resonance frequency of ~110 kHz in liquid (Biolever mini, Olympus). During AFM imaging, FD curves were recorded at a frequency of 2 kHz applying a sinusoidal amplitude of 24 nm to the

dx.doi.org/10.1021/nl403232z | *Nano Lett.* 2013, 13, 5585−5593

piezoelectric element moving the sample vertically. High-resolution AFM images were taken at a scan rate of 0.65 Hz and a pixel size of 3 × 3 Å^2 (768 × 768 pixel at 230 nm × 230 nm scan size). The maximum deflection for each FD curve (imaging force) was preset to 150 pN with an accuracy of 5−7 pN.[32,64] Feedback-loop parameters of the AFM were adjusted to minimize the imaging force error and maximize the topographic resolution. FD-based AFM images were simultaneously recorded in trace and retrace scanning direction and saved in separate channels for the topograph, deformation, elastic modulus (DMT), and imaging force error. Deformation values were mapped at 70% (45 pN) of the imaging force (150 pN). Before and after recording FD curves of the OmpF membrane, we recorded FD curves on the supporting mica to see whether the AFM tip contaminated. In the case of contaminations FD curves recorded on mica changed significantly in shape and reproducibility. To brush off contaminations from the AFM tip the mica was scanned at high speed and modulating the forces applied to the AFM cantilever.[48]

Averaging of FD-Based AFM Images. High-resolution FD-based AFM topographs and deformation channels simultaneously recorded of densely packed OmpF trimers were cross-correlation averaged using the SEMPER image processing system as described.[32] Briefly, unit cells of individual OmpF trimers were localized and extracted from high-resolution topographs, cross-correlated, averaged, and symmetrized. Position and orientation of every OmpF trimer as revealed from analyzing the FD-based AFM topographs were taken to extract and orient unit cells from the deformation channel. For each channel, the unit cells were then averaged and symmetrized.

Averaging of FD Curves. Individual FD curves recorded from the extracellular and the periplasmic surface of OmpF were exported as text file using the FD-based AFM data processing software (NanoScope Analysis, Bruker). FD curve text files were transferred to MatLab (MathWorks Corporation). The baseline of each FD curve was brought to zero force (offset correction) and the tip−sample distance was approximated from the vertical piezo movement minus the cantilever deflection.[31] FD curves recorded of the extracellular and periplasmic OmpF surface were separately aligned at their first data point and superimposed. From the superimposed FD curves, a density map was calculated using MatLab with data points being colored according to their density.

Computation of the Electrostatic Potential. To compute the electrostatic potential of the OmpF trimer, the X-ray structure of the trimer (PDB identifier 1OPF)[40] was embedded into a DMPC bilayer[65] consisting of 512 DMPC molecules and equilibrated at 303 K (Supporting Information Figure S3). Embedding was carried out using the g_membed module[66] of the GROMACS simulation suite version 4.5.4[67,68] and the Amber99-ildn-sb* extensions[69] to the Amber99 force field. Amber99 force field parameters of DMPC lipids were taken as published.[65,70] Electrostatics computations were carried out using the adaptive Poisson−Boltzmann solver (APBS) interface of the visual molecular dynamics software VMD on 2,146,689 grid points.[71] Mobile ion concentrations were considered implicitly. The APBS pqr input files were generated with editconf (www.gromacs.org). Solutions were obtained using the FEtk finite element solver.[72] Equipotential surfaces were obtained by interpolating between grid points having the same electrostatic potential and overlaid to the solvent accessible surface of the trimers (Figures 3 and Supporting Information Figure S4).[73]

■ ASSOCIATED CONTENT

Ⓢ Supporting Information

Schematics showing the principles of FD-based AFM (Figure S1), SDS gel of OmpF trimers purified from *Escherichia coli* (Figure S2), all-atom setup used to calculate the electrostatic potential generated by the OmpF trimer (Figure S3), electrostatic potential calculated of the OmpF trimer at different electrolyte concentrations (Figures S4), FD curves recorded on the extracellular and the periplasmic surface of the OmpF trimer (Figures S5), and determination of the surface charge density of the silicon AFM tip (Figures S6). This material is available free of charge via the Internet at http://pubs.acs.org.

■ AUTHOR INFORMATION

Corresponding Author

*E-mail: daniel.mueller@bsse.ethz.ch.

Author Contributions

M.P. build up the AFM setup, performed the experiments, and analyzed the data. U.H. setup the atomistic model of OmpF and lipid membrane and calculated the electrostatic potential. D.J.M. advised M.P. and U.H. and coanalyzed the calculated and experimental data. M.P., U.H., and D.J.M. wrote the paper.

Notes

The authors declare no competing financial interests.

■ ACKNOWLEDGMENTS

We thank C. Bippes, P. Bosshart, D. Martinez-Martin, I. Medalsy, R. Newton, and J. Thoma for experimental assistance, critical discussion and/or reading of the manuscript. The Swiss national science foundation (SNF) and the Klaus-Tschira Foundation supported this work.

■ ABBREVIATIONS

AFM, atomic force microscopy; FD curve, force−distance curve; FD-based AFM, force−distance based AFM; FD curve-based AFM, force−distance curved-based AFM; FV-AFM, force−volume AFM; OmpF, outer membrane protein F; DTT, dithiothreitol; DMPC, 1,2-dimyristoyl-sn-glycero-3-phosphorylcholine; HEPES, (4-(2-hydroxyethyl)-1-piperazineethanesulfonic acid); LDAO, *n*-dodecyl-*N*,*N*-dimethylamine-*N*-oxide; Octyl POE, *n*-octylpolyoxyethylene; SDS-PAGE, sodium dodecyl sulfate polyacrylamide gel electrophoresis; 2D, two-dimensional; 3D, three-dimensional

■ REFERENCES

(1) Fujiyoshi, Y.; Mitsuoka, K.; de Groot, B. L.; Philippsen, A.; Grubmuller, H.; Agre, P.; Engel, A. Structure and function of water channels. *Curr. Opin. Struct. Biol.* **2002**, *12*, 509−515.

(2) Gouaux, E.; Mackinnon, R. Principles of selective ion transport in channels and pumps. *Science* **2005**, *310*, 1461−1465.

(3) Bayley, H.; Cremer, P. S. Stochastic sensors inspired by biology. *Nature* **2001**, *413*, 226−230.

(4) Hou, X.; Guo, W.; Jiang, L. Biomimetic smart nanopores and nanochannels. *Chem. Soc. Rev.* **2011**, *40*, 2385−2401.

(5) Kowalczyk, S. W.; Blosser, T. R.; Dekker, C. Biomimetic nanopores: learning from and about nature. *Trends Biotechnol.* **2011**, *29*, 607−614.

(6) Maffeo, C.; Bhattacharya, S.; Yoo, J.; Wells, D.; Aksimentiev, A. Modeling and simulation of ion channels. *Chem. Rev.* **2012**, *112*, 6250−6284.
(7) Nakamura, H. Roles of electrostatic interaction in proteins. *Q. Rev. Biophys.* **1996**, *29*, 1−90.
(8) Roux, B.; MacKinnon, R. The cavity and pore helices in the KcsA K+ channel: Electrostatic stabilization of monovalent cations. *Science* **1999**, *285*, 100−102.
(9) Binnig, G.; Quate, C. F.; Gerber, C. Atomic force microscope. *Phys. Rev. Lett.* **1986**, *56*, 930−933.
(10) Gerber, C.; Lang, H. P. How the doors to the nanoworld were opened. *Nat. Nanotechnol.* **2006**, *1*, 3−5.
(11) Hoh, J. H.; Lal, R.; John, S. A.; Revel, J.-P.; Arnsdorf, M. F. Atomic force microscopy and dissection of gap junctions. *Science* **1991**, *253*, 1405−1408.
(12) Müller, D. J.; Schabert, F. A.; Büldt, G.; Engel, A. Imaging purple membranes in aqueous solutions at sub-nanometer resolution by atomic force microscopy. *Biophys. J.* **1995**, *68*, 1681−1686.
(13) Schabert, F. A.; Henn, C.; Engel, A. Native *Escherichia coli* OmpF porin surfaces probed by atomic force microscopy. *Science* **1995**, *268*, 92−94.
(14) Engel, A.; Müller, D. J. Observing single biomolecules at work with the atomic force microscope. *Nat. Struct. Biol.* **2000**, *7*, 715−718.
(15) Muller, D. J. AFM: a nanotool in membrane biology. *Biochemistry* **2008**, *47*, 7986−7998.
(16) Müller, D. J.; Baumeister, W.; Engel, A. Conformational change of the hexagonally packed intermediate layer of *Deinococcus radiodurans* imaged by atomic force microscopy. *J. Bacteriol.* **1996**, *178*, 3025−3030.
(17) Müller, D. J.; Hand, G. M.; Engel, A.; Sosinsky, G. Conformational changes in surface structures of isolated Connexin26 gap junctions. *EMBO J.* **2002**, *21*, 3598−3607.
(18) Yu, J.; Bippes, C. A.; Hand, G. M.; Muller, D. J.; Sosinsky, G. E. Aminosulfonate modulated pH-induced conformational changes in connexin26 hemichannels. *J. Biol. Chem.* **2007**, *282*, 8895−8904.
(19) Shibata, M.; Yamashita, H.; Uchihashi, T.; Kandori, H.; Ando, T. High-speed atomic force microscopy shows dynamic molecular processes in photoactivated bacteriorhodopsin. *Nat. Nanotechnol.* **2010**, *5*, 208−212.
(20) Shibata, M.; Uchihashi, T.; Yamashita, H.; Kandori, H.; Ando, T. Structural changes in bacteriorhodopsin in response to alternate illumination observed by high-speed atomic force microscopy. *Angew. Chem., Int. Ed.* **2011**, *50*, 4410−4413.
(21) Mari, S. A.; Pessoa, J.; Altieri, S.; Hensen, U.; Thomas, L.; Morais-Cabral, J. H.; Muller, D. J. Gating of the MlotiK1 potassium channel involves large rearrangements of the cyclic nucleotide-binding domains. *Proc. Natl. Acad. Sci. U.S.A.* **2011**, *108*, 20802−20807.
(22) Sumino, A.; Sumikama, T.; Iwamoto, M.; Dewa, T.; Oiki, S. The open gate structure of the membrane-embedded KcsA potassium channel viewed from the cytoplasmic side. *Sci. Rep.* **2013**, *3*, 1063.
(23) Shinozaki, Y.; Sumitomo, K.; Tsuda, M.; Koizumi, S.; Inoue, K.; Torimitsu, K. Direct observation of ATP-induced conformational changes in single P2X(4) receptors. *PLoS Biol.* **2009**, *7*, e1000103.
(24) Müller, D. J.; Engel, A. Voltage and pH-induced channel closure of porin OmpF visualized by atomic force microscopy. *J. Mol. Biol.* **1999**, *285*, 1347−1351.
(25) Mari, S. A.; Koster, S.; Bippes, C. A.; Yildiz, O.; Kuhlbrandt, W.; Muller, D. J. pH-induced conformational change of the beta-barrel-forming protein OmpG reconstituted into native E. coli lipids. *J. Mol. Biol.* **2010**, *396*, 610−616.
(26) Muller, D. J.; Dufrene, Y. Atomic force microscopy as a multifunctional molecular toolbox in nanobiotechnology. *Nat. Nanotechnol.* **2008**, *3*, 261−269.
(27) Radmacher, M.; Cleveland, J. P.; Fritz, M.; Hansma, H. G.; Hansma, P. K. Mapping interaction forces with the atomic force microscope. *Biophys. J.* **1994**, *66*, 2159−2165.
(28) Ludwig, M.; Dettmann, W.; Gaub, H. E. Atomic force microscope imaging contrast based on molecular recognition. *Biophys. J.* **1997**, *72*, 445−448.
(29) Heinz, W. F.; Hoh, J. H. Spatially resolved force spectroscopy of biological surfaces using the atomic force microscope. *Trends Biotechnol.* **1999**, *17*, 143−150.
(30) Dufrene, Y. F.; Martinez-Martin, D.; Medalsy, I.; Alsteens, D.; Muller, D. J. Multiparametric imaging of biological systems by force-distance curve-based AFM. *Nat. Methods* **2013**, *10*, 847−854.
(31) Butt, H. J.; Cappella, B.; Kappl, M. Force measurements with the atomic force microscope: Technique, interpretation and applications. *Surf. Sci. Rep.* **2005**, *59*, 1−152.
(32) Medalsy, I.; Hensen, U.; Muller, D. J. Imaging and quantifying chemical and physical properties of native proteins at molecular resolution by force-volume AFM. *Angew. Chem., Int. Ed.* **2011**, *50*, 12103−12108.
(33) Rico, F.; Su, C.; Scheuring, S. Mechanical mapping of single membrane proteins at submolecular resolution. *Nano Lett.* **2011**, *11*, 3983−3986.
(34) Thoma, J.; Bosshart, P.; Pfreundschuh, M.; Muller, D. J. Out but not In: The large transmembrane beta-barrel protein FhuA unfolds but cannot refold via beta-hairpins. *Structure* **2012**, *20*, 2185−2190.
(35) Wegmann, S.; Medalsy, I. D.; Mandelkow, E.; Muller, D. J. The fuzzy coat of pathological human Tau fibrils is a two-layered polyelectrolyte brush. *Proc. Natl. Acad. Sci. U.S.A.* **2013**, *110*, E313−321.
(36) Zhang, S.; Andreasen, M.; Nielsen, J. T.; Liu, L.; Nielsen, E. H.; Song, J.; Ji, G.; Sun, F.; Skrydstrup, T.; Besenbacher, F.; Nielsen, N. C.; Otzen, D. E.; Dong, M. Coexistence of ribbon and helical fibrils originating from hIAPP(20−29) revealed by quantitative nanomechanical atomic force microscopy. *Proc. Natl. Acad. Sci. U.S.A.* **2013**, *110*, 2798−2803.
(37) Israelachvili, J. *Intermolecular and Surface Forces*, 2nd ed.; Academic Press Limited: London, 1991.
(38) Butt, H. J. Measuring electrostatic, van der Waals, and hydration forces in electrolyte solutions with an atomic force microscope. *Biophys. J.* **1991**, *60*, 1438−1444.
(39) Butt, H. J. Measuring local surface charge densities in electrolyte solutions with a scanning force microscope. *Biophys. J.* **1992**, *63*, 578−582.
(40) Cowan, S. W.; Schirmer, T.; Rummel, G.; Steiert, M.; Ghosh, R.; Pauptit, R. A.; Jansonius, J. N.; Rosenbusch, J. P. Crystal structures explain functional properties of two *E. coli* porins. *Nature* **1992**, *358*, 727−733.
(41) Koebnik, R.; Locher, K. P.; Van Gelder, P. Structure and function of bacterial outer membrane proteins: barrels in a nutshell. *Mol. Microbiol.* **2000**, *37*, 239−253.
(42) Nikaido, H. Molecular basis of bacterial outer membrane permeability revisited. *Microbiol. Mol. Biol. Rev.* **2003**, *67*, 593−656.
(43) Schirmer, T. General and specific porins from bacterial outer membranes. *J. Struct. Biol.* **1998**, *121*, 101−109.
(44) Schirmer, T.; Phale, P. S. Brownian dynamics simulation of ion flow through porin channels. *J. Mol. Biol.* **1999**, *294*, 1159−1167.
(45) Saint, N.; Lou, K. L.; Widmer, C.; Luckey, M.; Schirmer, T.; Rosenbusch, J. P. Structural and functional characterization of OmpF porin mutants selected for larger pore size. II. Functional characterization. *J. Biol. Chem.* **1996**, *271*, 20676−20680.
(46) Klebba, P. E.; Newton, S. M. C. Mechanisms of solute transport through outer membrane porins: burning down the house. *Curr. Opin. Microbiol.* **1998**, *1*, 238−247.
(47) Philippsen, A.; Im, W.; Engel, A.; Schirmer, T.; Roux, B.; Muller, D. J. Imaging the electrostatic potential of transmembrane channels: atomic probe microscopy of OmpF porin. *Biophys. J.* **2002**, *82*, 1667−1676.
(48) Muller, D. J.; Engel, A. Atomic force microscopy and spectroscopy of native membrane proteins. *Nat. Protoc.* **2007**, *2*, 2191−2197.
(49) Muller, D. J.; Engel, A. The height of biomolecules measured with the atomic force microscope depends on electrostatic interactions. *Biophys. J.* **1997**, *73*, 1633−1644.

(50) Yildiz, O.; Vinothkumar, K. R.; Goswami, P.; Kuhlbrandt, W. Structure of the monomeric outer-membrane porin OmpG in the open and closed conformation. *EMBO J.* **2006**, *25*, 3702−3713.
(51) Andersen, C.; Schiffler, B.; Charbit, A.; Benz, R. PH-induced collapse of the extracellular loops closes Escherichia coli maltoporin and allows the study of asymmetric sugar binding. *J. Biol. Chem.* **2002**, *277*, 41318−41325.
(52) Engel, A.; Schoenenberger, C. A.; Muller, D. J. High resolution imaging of native biological sample surfaces using scanning probe microscopy. *Curr. Opin. Struct. Biol.* **1997**, *7*, 279−284.
(53) Müller, D. J.; Fotiadis, D.; Scheuring, S.; Müller, S. A.; Engel, A. Electrostatically balanced subnanometer imaging of biological specimens by atomic force microscopy. *Biophys. J.* **1999**, *76*, 1101−1111.
(54) Stock, J. B.; Rauch, B.; Roseman, S. Periplasmic space in *Salmonella typhimurium* and *Escherichia coli*. *J. Biol. Chem.* **1977**, *252*, 7850−7861.
(55) Sen, K.; Hellman, J.; Nikaido, H. Porin channels in intact cells of *Escherichia coli* are not affected by donnan potentials across the outer membrane. *J. Biol. Chem.* **1988**, *263*, 1182−1187.
(56) Sheinerman, F. B.; Norel, R.; Honig, B. Electrostatic aspects of protein-protein interactions. *Curr. Opin. Struct. Biol* **2000**, *10*, 153−159.
(57) Whorton, M. R.; MacKinnon, R. X-ray structure of the mammalian GIRK2-betagamma G-protein complex. *Nature* **2013**, *498*, 190−197.
(58) McLaughlin, S. The electrostatic properties of membranes. *Annu. Rev. Biophys. Biophys. Chem.* **1989**, *18*, 113−136.
(59) Frederix, P. L. T. M.; Gullo, M. R.; Akiyama, T.; Tonin, A.; de Rooij, N. F.; Staufer, U.; Engel, A. Assessment of insulated conductive cantilevers for biology and electrochemistry. *Nanotechnology* **2005**, *16*, 997−1005.
(60) Frisbie, C. D.; Rozsnyai, L. F.; Noy, A.; Wrighton, M. S.; Lieber, C. M. Functional group imaging by chemical force microscopy. *Science* **1994**, *265*, 2071−2074.
(61) Dague, E.; Alsteens, D.; Latge, J. P.; Verbelen, C.; Raze, D.; Baulard, A. R.; Dufrene, Y. F. Chemical Force Microscopy of Single Live Cells. *Nano Lett.* **2007**, *7*, 3026−3030.
(62) Holzenburg, A.; Engel, A.; Kessler, R.; Manz, H. J.; Lustig, A.; Aebi, U. Rapid Isolation of OmpF porin-LPS Complexes Suitable for Structure-Function Studies. *Biochemistry* **1989**, *28*, 4187−4193.
(63) Remigy, H. W.; Caujolle-Bert, D.; Suda, K.; Schenk, A.; Chami, M.; Engel, A. Membrane protein reconstitution and crystallization by controlled dilution. *FEBS Lett.* **2003**, *555*, 160−169.
(64) Medalsy, I. D.; Muller, D. J. Nanomechanical Properties of Proteins and Membranes Depend on Loading Rate and Electrostatic Interactions. *ACS Nano* **2013**, *7*, 2642−2650.
(65) Jambeck, J. P.; Lyubartsev, A. P. Derivation and Systematic Validation of a Refined All-Atom Force Field for Phosphatidylcholine Lipids. *J. Phys. Chem. B* **2012**, *116*, 3164−3179.
(66) Wolf, M. G.; Hoefling, M.; Aponte-Santamaria, C.; Grubmuller, H.; Groenhof, G. g_membed: Efficient Insertion of a Membrane Protein into an Equilibrated Lipid Bilayer with Minimal Perturbation. *J. Comput. Chem.* **2010**, *31*, 2169−2174.
(67) Berendsen, H. J. C.; Vanderspoel, D.; Vandrunen, R. Gromacs - a Message-Passing Parallel Molecular-Dynamics Implementation. *Comput. Phys. Commun.* **1995**, *91*, 43−56.
(68) Hess, B.; Kutzner, C.; van der Spoel, D.; Lindahl, E. GROMACS 4: Algorithms for highly efficient, load-balanced, and scalable molecular simulation. *J. Chem. Theory Comput.* **2008**, *4*, 435−447.
(69) Lindorff-Larsen, K.; Piana, S.; Palmo, K.; Maragakis, P.; Klepeis, J. L.; Dror, R. O.; Shaw, D. E. Improved side-chain torsion potentials for the Amber ff99SB protein force field. *Proteins: Struct., Funct., Bioinf.* **2010**, *78*, 1950−1958.
(70) Klauda, J. B.; Venable, R. M.; Freites, J. A.; O'Connor, J. W.; Tobias, D. J.; Mondragon-Ramirez, C.; Vorobyov, I.; MacKerell, A. D., Jr.; Pastor, R. W. Update of the CHARMM All-Atom Additive Force Field for Lipids: Validation on Six Lipid Types. *J. Phys. Chem. B* **2010**, *114*, 7830−7843.
(71) Baker, N. A.; Sept, D.; Joseph, S.; Holst, M. J.; McCammon, J. A. Electrostatics of nanosystems: application to microtubules and the ribosome. *Proc. Natl. Acad. Sci. U.S.A.* **2001**, *98*, 10037−10041.
(72) Holst, M. Adaptive numerical treatment of elliptic systems on manifolds. *Adv. Comput. Math.* **2001**, *15*, 139−191.
(73) Varshney, A.; Brooks, F. P.; Wright, W. V. Linearly scalable computation of smooth molecular surfaces. *IEEE Comp. Graph. Appl.* **1994**, *14*, 19−25.

Quantitative imaging of the electrostatic field and potential generated by a transmembrane protein pore at sub-nanometer resolution

Moritz Pfreundschuh, Ulf Hensen & Daniel J. Müller

SUPPORTING INFORMATION

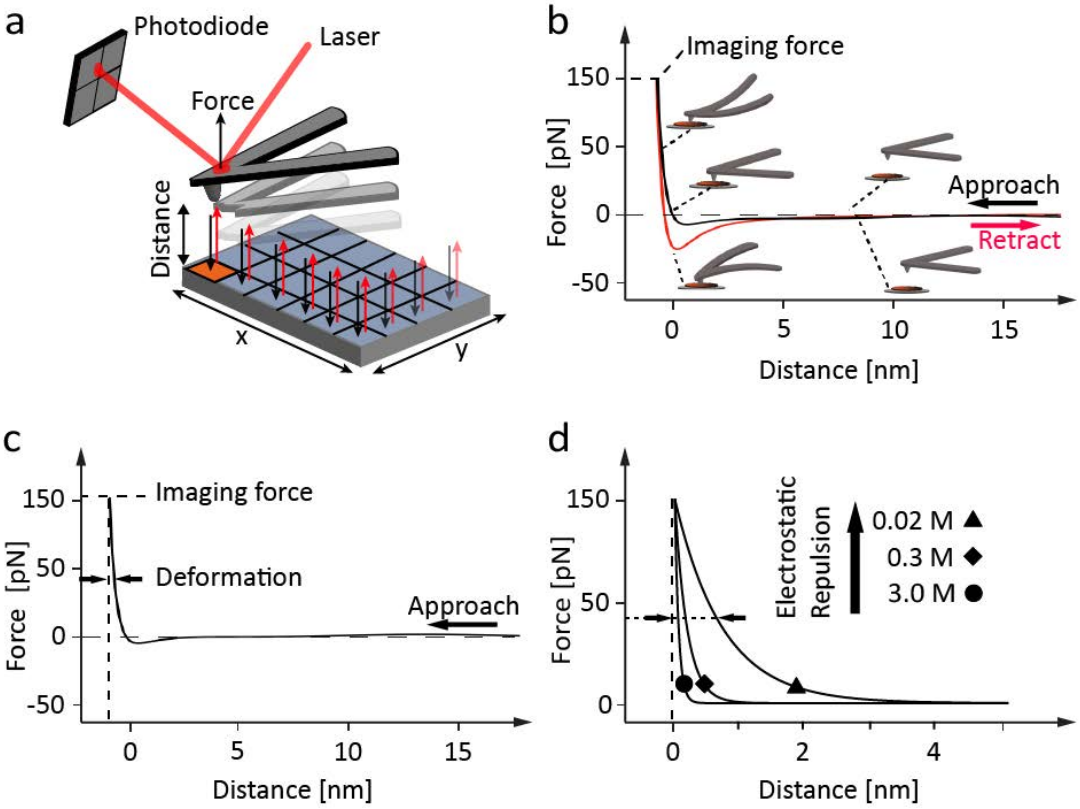

Figure 1. Principles of force-distance (FD) curve based AFM. FD-based AFM contours the sample surface (**a**) and pixel-by-pixel approaches (black arrow) and retracts (red arrow) AFM tip and sample to record FD curves (**b**). The AFM cantilever deflection measures the force interacting between AFM tip and sample. Attractive forces pull the AFM tip toward the sample and the cantilever deflects downward (negative). Repulsive forces between AFM tip and sample deflect the cantilever upward (positive). To record the sample topography at a preset force, the AFM tip is pressed onto the sample until a preset maximum contact force (imaging force) is reached, which triggers the reverse movement (retraction) of the tip.[1] Finally, the sample topography is contoured at the imaging force. (**c**) The mechanical deformation of a soft biological sample is described by the indentation of the much stiffer AFM tip. This indentation is detected as repulsive force. Conventionally, deformation values give the distance recorded at the imaging force (here 150 pN) minus the distance recorded at a given threshold force (here 45 pN). '0 nm' approximates the contact between AFM tip and sample. (**d**) Exemplified FD curves recorded between a stiff silicon nitride AFM tip and stiff freshly cleaved mica in aqueous solution containing 0.02, 0.3 or 3 M monovalent electrolyte.[2] The force applied to record the FD curves was too small to mechanically deform mica. The shapes of the FD curves demonstrate that the electrostatic repulsion between AFM tip and sample (mica) depends on the electrolyte concentration. In the case shown, increasing the electrolyte concentration decreases the electrostatic double layer repulsion.[2] Thus, the 'deformation value' of FD curves can measure electrostatic repulsion[3].

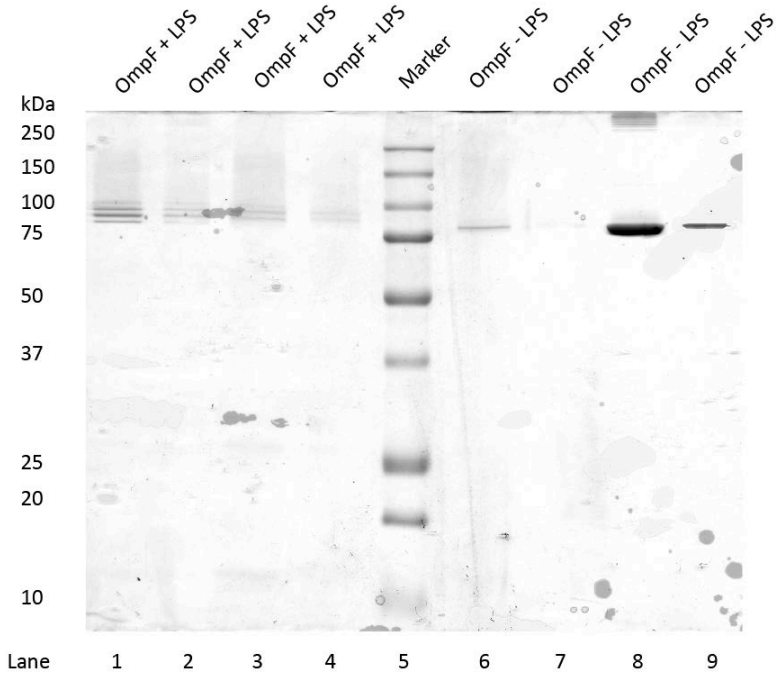

Supporting Figure S2. SDS gel of OmpF trimers purified from *Escherichia coli*. SDS-PAGE gel of purified and solubilized OmpF (in 1% (w/v) Octyl POW) before (lanes 1-4) and after (lanes 5-8) treatment with 100 mM EDTA in 1% (w/v) LDAO for 4h at room temperature. Electrophoresis was performed at room temperature using 12% separating and 5% stacking gels. Gels were stained with coomassie brilliant blue. Purified OmpF migrates at a mass of ≈80 kDa, which corresponds to the calculated mass of 117 kDa of the transmembrane OmpF trimer[4]. The ladder-like pattern of OmpF (lane 1-4) corresponds to increasing numbers of lipopolysaccharides (LPS) bound to the outer membrane protein[5]. Applied OmpF concentrations were between 0.5 and 4.0 µg per lane.

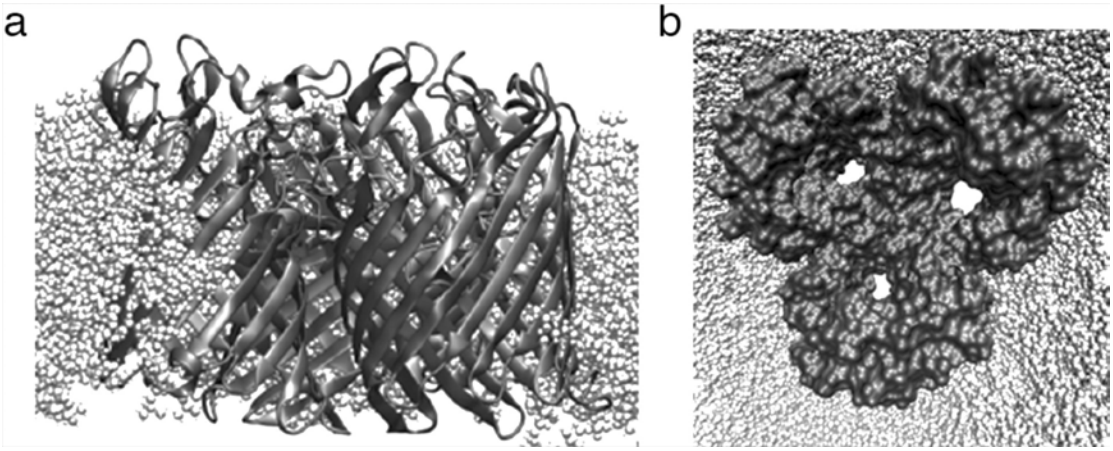

Supporting Figure S3. All-atom setup used to calculate the electrostatic potential generated by the OmpF trimer at different electrolyte concentrations. (**a**) Side view of the OmpF trimer (PDB entry file 1OPF)[6] embedded into a lipid (DMPC) membrane. The top shows the extracellular and the bottom the periplasmic surface of the OmpF trimer. All atoms of the lipids and the backbone of the OmpF trimer are displayed. (**b**) Top view on the periplasmic surface. All atoms of the lipids and the surface of the OmpF trimer are displayed.

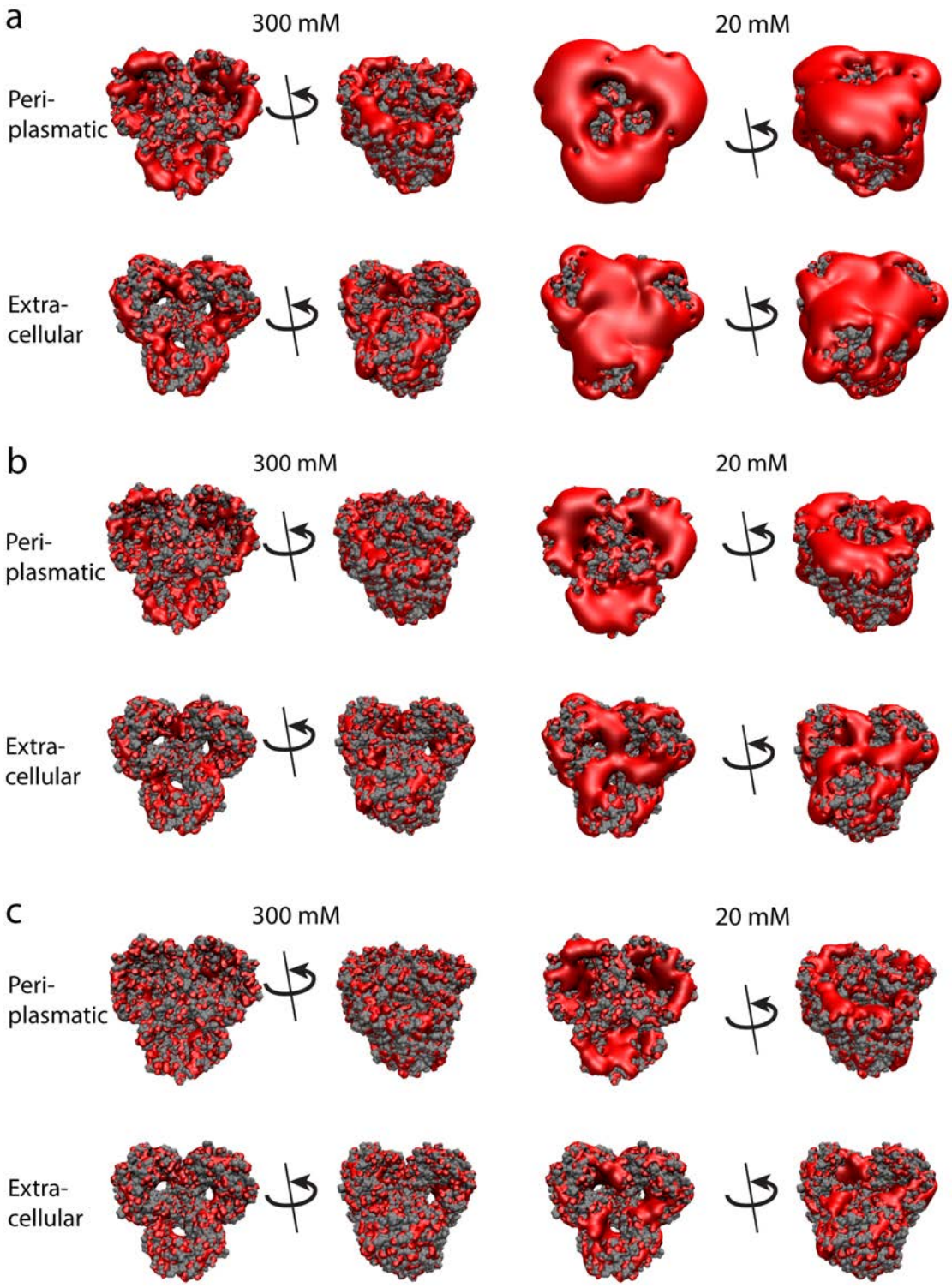

Supporting Figure S4. Electrostatic potential calculated of the OmpF trimer at different electrolyte concentrations. The negative electrostatic potential of the OmpF trimer calculated for 300 mM and 20 mM monovalent electrolyte is displayed using equipotential surfaces at (**a**) –35 mV, (**b**) –67 mV, and (**c**) –101 mV. Shown are the top and tilted views of the periplasmic and extracellular surface of the OmpF trimer.

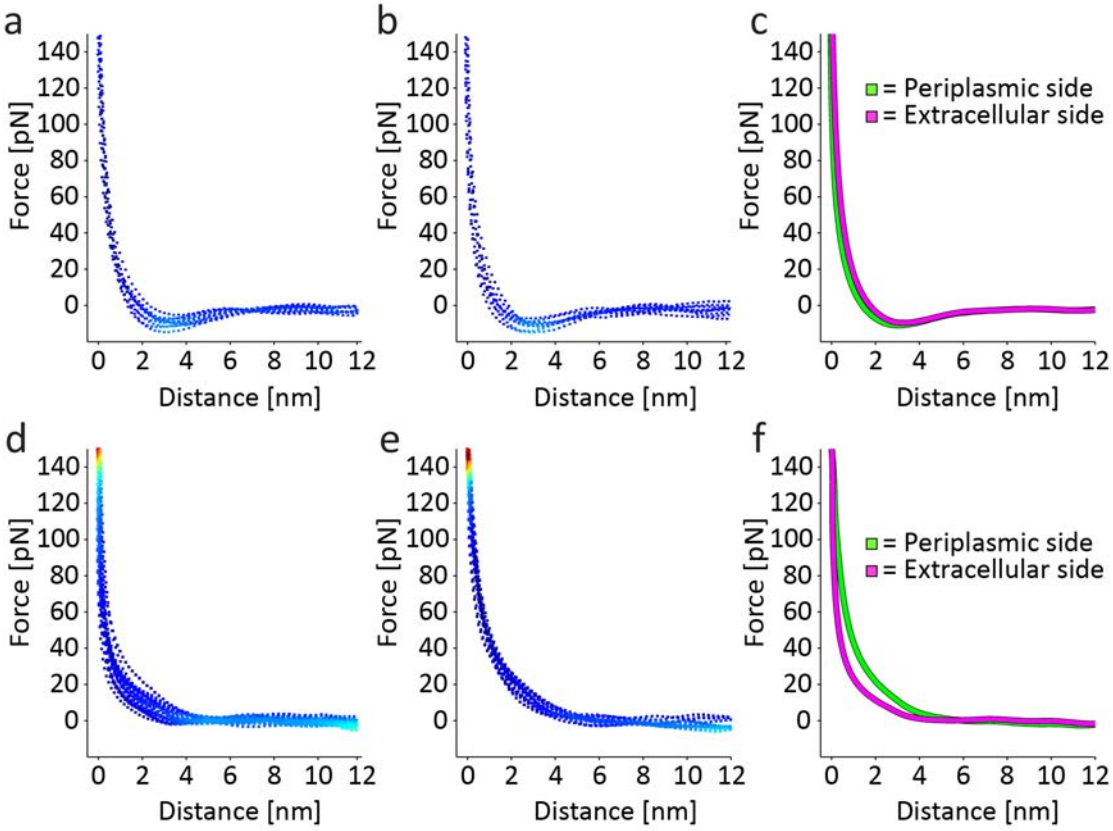

Supporting Figure S5. FD curves recorded on the extracellular and the periplasmic surface of the OmpF trimer. 100 FD curves were extracted on the periplasmic and extracellular surface of OmpF from high-resolution FD-based AFM images recorded at high (**a-c**) and low (**d-f**) electrolyte. (**a**) and (**d**) show the FD curves as density plot derived from the extracellular surface, (**b**) and (**e**) from the periplasmic surface, respectively. (**c**) and (**f**) show the averages of the FD curves recorded at the periplasmic (green) and extracellular (purple) surface of the OmpF trimer.

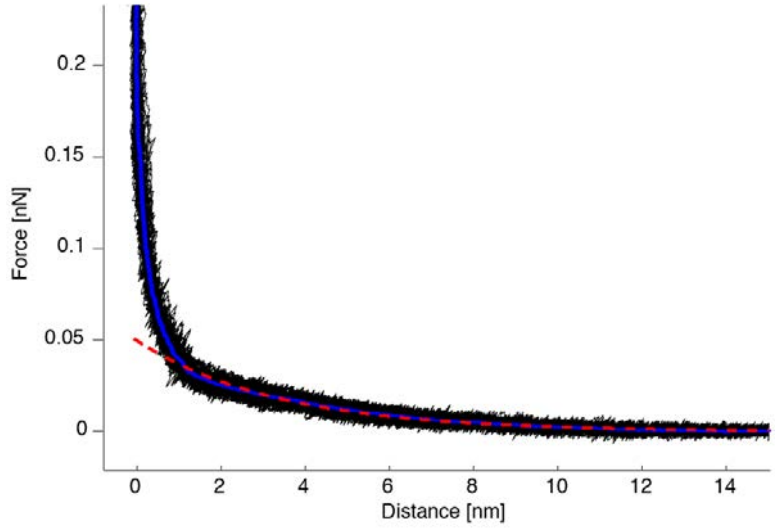

Supporting Figure S6. Determining the surface charge density of the silicon AFM tip by recording FD curves on mica in electrolyte solution. Shown is an average FD curve that has been calculated from 1,000 superimposed FD curves. The data points of the superimposed 1,000 FD curves are shown in black and their average in blue. Every single FD curve has been recorded approaching the silicon tip of the AFM cantilever (BioLever mini) to freshly cleaved mica in aqueous solution (ultrapure water, >18 MOhm/cm) containing 3 mM KCl electrolyte. The 1,000 FD curves have been recorded on five different locations on the mica surface at 0.5 Hz acquisition rate, 44 data points/nm, and applying a maximal force of 0.4 nN.

The electrostatic double layer force interacting between the AFM tip and mica in electrolyte solution can be described as following:[7,8]

$$F_{el}(D) = \frac{4*\pi*R*\sigma_S*\sigma_T*\lambda}{\epsilon_0*\epsilon_r} * e^{-D/\lambda} \qquad \text{Equation S1}$$

with the nominal tip radius $R \approx 10$ nm* (BioLever mini), the Debye length $\lambda = 0.304/(0.003^{1/2})$ nm, the surface charge density of mica in 3 mM KCl is $\sigma_S = -0.009$ C/m^2 [ref. [9]] the distance between AFM tip and mica D, the permittivity of vacuum $\varepsilon_0 = 8.854\ 10^{-12}$ C/Vm, the relative permittivity of water $\varepsilon_r = 80.1$, and the surface charge density of the AFM tip σ_T. Accordingly, the charge density of the AFM tip can be determined at $D = 0$ nm plotting $\sigma_T = \left(\frac{F_{el}(0)*\epsilon_0*\epsilon_r}{4*\pi*R*\sigma_S*\lambda}\right)$. However, because the absolute distance between AFM tip and mica surface is difficult to determine,[2] we fitted the FD curve using Eq. S1 using the parameters given above to determine σ_T. The fitted curve is shown in red dashes. Measurements and analysis were repeated five times using five different AFM cantilevers. The fits revealed a surface charge density of the silicon AFM tips (Biolever mini) of –0.032 ± 0.010 C/m^2 (n = 5).

* The nominal tip radius taken for determining the surface charge density of the AFM tip was larger compared to the tip radius used for high-resolution AFM imaging (see main manuscript). The reason was that the electrostatic double layer interaction extends over several nanometers, whereas the interaction contributing to high-resolution AFM images must be much more localized to be able to contour the sample surface a sub-nanometer resolution[10,11].

Supporting References

(1) Medalsy, I.; Hensen, U.; Muller, D. J. Imaging and quantifying chemical and physical properties of native proteins at molecular resolution by force-volume AFM. *Angew Chem Int Ed Engl* **2011,** 50, 12103-12108.
(2) Butt, H. J.; Cappella, B.; Kappl, M. Force measurements with the atomic force microscope: Technique, interpretation and applications. *Surf Sci Rep* **2005,** 59, 1-152.
(3) Medalsy, I. D.; Muller, D. J. Nanomechanical properties of proteins and membranes depend on loading rate and electrostatic interactions. *ACS Nano* **2013,** 7, 2642-2650.
(4) Ziervogel, B. K.; Roux, B. The binding of antibiotics in OmpF porin. *Structure* **2013,** 21, 76-87.
(5) Locher, K. P.; Rosenbusch, J. P. Oligomeric states and siderophore binding of the ligand-gated FhuA protein that forms channels across Escherichia coli outer membranes. *Eur J Biochem* **1997,** 247, 770-775.
(6) Cowan, S. W.; Schirmer, T.; Rummel, G.; Steiert, M.; Ghosh, R.; Pauptit, R. A.; Jansonius, J. N.; Rosenbusch, J. P. Crystal structures explain functional properties of two *E. coli* porins. *Nature* **1992,** 358, 727-733.
(7) Israelachvili, J., *Intermolecular & surface forces*. Second Edition ed.; Academic Press Limited: London, 1991.
(8) Butt, H. J. Measuring local surface charge densities in electrolyte solutions with a scanning force microscope. *Biophys J* **1992,** 63, 578-582.
(9) Pashley, R. M. Hydration forces between mica surfaces in aqueous electrolyte solutions. *J Colloid Interface Sci* **1981,** 80, 153-162.
(10) Engel, A.; Schoenenberger, C. A.; Muller, D. J. High resolution imaging of native biological sample surfaces using scanning probe microscopy. *Curr Opin Struct Biol* **1997,** 7, 279-284.
(11) Müller, D. J.; Fotiadis, D.; Scheuring, S.; Müller, S. A.; Engel, A. Electrostatically balanced subnanometer imaging of biological specimens by atomic force microscopy. *Biophys J* **1999,** 76, 1101-1111.